Schweizerische Eidgenossenschaft
Confédération suisse
Confederazione Svizzera
Confederaziun svizra

Eidgenössisches Departement für
Umwelt, Verkehr, Energie und Kommunikation UVEK

Bundesamt für Energie BFE

Schlussbericht 30. August 2010

Construction and modelling of a thermoelectric oxide module (TOM) as a demonstrator

Auftraggeber:
Bundesamt für Energie BFE
Forschungsprogramm Elektrizitätstechnologien & -anwendungen
CH-3003 Bern
www.bfe.admin.ch

Kofinanzierung:
Empa, 8600 Dübendorf

V-ZUG, 6301 Zug

Auftragnehmer:
EMPA Dübendorf
Überlandstrasse 129
CH-8600 Dübendorf
www.empa.ch

Autoren:
Petr Tomeš, EMPA, petr.tomes@empa.ch
Anke Weidenkaff, EMPA, anke.weidenkaff@empa.ch

BFE-Bereichsleiter: Dr. Michael Moser
BFE-Programmleiter: Roland Brüniger
BFE-Vertrags- und Projektnummer: 152820 / 101356

Table of contents

Zusammenfassung

Das Ziel dieses Projektes war die Entwicklung verbesserter thermoelektrischer (TE) Materialien für die direkte Umwandlung von Sonnenwärme in Elektrizität. Die maximale Leistungsabgabe P_{max} und der Wirkungsgrad η der Umwandlung wurde bei mehreren vierbeinigen thermoelektrischen oxidischen Modulen (TOM) bestimmt. Die Module bestanden aus je zwei *p*- ($La_{1.98}Sr_{0.02}CuO_4$) und zwei *n*- ($CaMn_{0.98}Nb_{0.02}O_3$) Thermoelementen, welche elektrisch in Serie und thermisch parallel geschaltet waren. Die Sonnenwärme lieferte eine High-Flux Solar Simulator Source (HFSS), welche ein sonnenähnliches Strahlungsspektrum erzeugt. Unsere Messungen sind als Machbarkeitsstudie für die Nutzung von Hochtemperatursolarstrahlung gedacht. Bisher scheiterten derartige Untersuchungen an der geringen Temperaturstabilität konventioneller TE-Materialien. Die vorliegende Studie beweist, dass die Module zur direkten Umwandlung von Sonnenwärme in der Lage sind. Die Messungen zeigen einen nahezu linearen Temperaturgradienten durch den Modulquerschnitt. Allerdings betrug die maximal erzielte Leitungsabgabe nur 88.8 mW bei einem TOM mit 5 mm Beinlänge und einer Temperaturdifferenz von $\Delta T = 622$ K und muss noch durch die Anpassung des Konverterdesigns and die angewendeten Materialien optimiert werden. Der höchste Umwandlungswirkungsgrad η wurde bei einem Wärmefluss von 4 – 8 W cm^{-2} gemessen. Die Abhängigkeit des Wirkungsgrads η von der Beinlänge der Module wurde ebenso untersucht wie der Einfluss eines Graphitüberzugs auf der Al_2O_3-Oberfläche der heissen Modulseite auf ΔT, P_{max} and η.

Abstract

The project aims at the development of better thermoelectric materials for the direct conversion of solar heat into electricity. The maximum output power P_{max} and the efficiency η of the conversion was measured on a series of four-leg thermoelectric oxide modules (TOM). The modules were constructed by combining two *p*- ($La_{1.98}Sr_{0.02}CuO_4$) and two *n*-type ($CaMn_{0.98}Nb_{0.02}O_3$) thermoelements connected electrically in series and thermally in parallel. The temperature gradient ΔT was provided by a High-Flux Solar Simulator source (HFSS) which generates a spectrum similar to solar radiation. This project was intended to be a feasibility study for the utilization of high temperature solar heat, which could not previously be demonstrated due to the low temperature stability of conventional materials. The direct conversion was proven by this study. The measurements show an almost linear temperature profile along the thermoelectric legs. However, the maximum output power resulted in 88.8 mW for a TOM with a leg length of 5 mm at $\Delta T = 622$ K. and has yet to be optimized by improving the converter design and the applied materials. The highest conversion efficiency η was found for a heat flux of 4 – 8 W cm^{-2}. The dependence of η on the leg length was studied as well as the influence of a graphite coating on the hot Al_2O_3 surface on ΔT, P_{max} and η.

1. Objectives

The decrease of fossil fuels has motivated many research groups to find alternative energy sources [1, 2]. Solar cells operating at 20 % efficiency and covering 0.1% of the earth's land area would give enough energy to supply the yearly worldwide energy demand [3]. Nevertheless existing technologies such as photovoltaics and solar thermal converters are leading to a low power output and various maintenance problems. The sun as energy source can also be used by thermoelectric (TE) modules, which directly convert heat (i.e. solar heat) into electricity. The advantage of TE modules compared to solar cells is that TE modules utilize the IR and part of the UV and visible radiation of the solar spectrum while solar cells only uses the UV spectrum [4]..

The performance of a thermoelectric material is specified by the Figure of Merit, $ZT = S^2T / \rho\kappa$, where S is the Seebeck coefficient, ρ is the electrical resistivity and κ is the thermal conductivity. A sufficient conversion efficiency η requires values of the Figure of Merit of at least of $ZT \sim 1$. The conversion efficiency is thermodynamically limited by the Carnot efficiency [5]. As it was shown by Yang & Caillat, a Figure of Merit in the range of $2 < ZT < 3$ leads to a conversion efficiency of ~ 50 % of the Carnot efficiency. Beside the properties of the thermoelectric materials the conversion efficiency also depends on the construction of the TE device.

Conventional thermoelectric devices are based on Bi_2Te_3 because this material exhibits a relatively high Figure of Merit [6-7]. Disadvantage of Bi_2Te_3 are its limited chemical stability at high temperatures and its toxicity. Therefore, complex metal oxides are promising alternatives for high temperature applications because they are stable at high temperatures in air and non-toxic [8-12]. Among these oxides, $Na_xCo_2O_4$ [13] is especially interesting as it shows a high Figure of Merit, ZT ~ 0.8 at T = 800 K [14]. The production of single crystal material and keeping a stable stoichiometry is difficult, though In contrast, perovskite – type materials based on manganate and cuprate can be easily synthesized with controllable TE properties and relatively cost-effective. The demonstration of the direct conversion of solar heat into electrical energy by a series of thermoelectric modules based on perovskite-type oxide materials is crucial to enhance interest in thermoelectricity.

However, development and understanding of the properties of the new promising unconventional materials is the goal of the present and the future work. The studied $Sr_{1-x}Na_xRuO_3$ and $PrCo_{1-x}Ni_xO_3$ ceramics belong to a large perovskite-type family studied since the 1940s [15, 16]. Perovskite-type systems based on copper have been intensively investigated in the 1990s because of their superconducting behavior. The colossal magneto resistance effect (CMR) of manganites was subject of intensive research more recently [17, 18]. Studies on double perovskites e.g. investigating the spin polarized carriers in Sr_2FeMoO_6 or checking the Ru valence in $La_{2-x}Sr_xCoRuO_6$ were carried out during the last decade [19, 20]. Physical properties of 4*d* and 5*d* metal oxides still represent a less explored area of research, though.

The orthorhombic $SrRuO_3$ belongs to the perovskite-type family as well. It shows the *Pbnm* space group, metallic conductivity and ferromagnetic behavior below $T_C \sim 160$ K [21]. The itinerant character of the ferromagnetism in $SrRuO_3$ is underlined by unsaturated magnetization under the high magnetic field and the character of conducting electrons ranks this material to the family of strongly electron - correlated systems [22]. Considering the robustness of the metallic ground state of $SrRuO_3$ with respect to both electron occupancy and crystal lattice distortion, we studied the highly homogeneous and crystallographically well characterized $Sr_{1-x}Na_xRuO_3$ ($0.0 \leq x \leq 0.19$) ceramics in order to localize possible magnetically polarized Ru 4*d* electrons when their density is decreased due to the charge compensation ($Sr^{2+} <=> Na^{1+}$).

The spin state of Co^{3+} ions in perovskite-type cobaltates can be low-spin (LS, $t_{2g}^6 e_g^0$), intermediate-spin (IS, $t_{2g}^5 e_g^1$) and high-spin (HS, $t_{2g}^4 e_g^2$). This multitude of the spin states dramatically influences the physical properties associated with magnetic and electronic transitions. Simultaneous changes in the crystal structure along with Jahn-Teller distortion of the CoO_6 octahedron are observed [23-24]. The paramagnetic insulators $PrCoO_3$ and $LaCoO_3$ are isoelectronic. However, $LaCoO_3$, the most studied rare-earth cobalt perovskite, has a rhombohedral crystal structure in contrast to the orthorhombic $PrCoO_3$ due to the smaller ionic radius of the Pr^{3+} ion [26]. The substitution of Co by Ni influences the character of the electronic transport which changes from variable range hopping (VRH) into nearest neighbor hopping (NNH) [27]. The dependence of the Seebeck coefficient of the Ni substitution follows the Heikes equation [28]. Hashimoto et al. investigated a direct relationship between the ionic radii of rare-earth elements in perovskite-type Ln oxides and their thermoelectric properties [14]. The orthorhombic perovskite $PrCoO_3$ with the space group *Pbnm* shows insulator-like conductivity and paramagnetic behavior in the temperature range of 4 K < T < 1000 K with an effective magnetic moment μ_{eff} = 3.41 μ_B which is close to the effective magnetic moment of μ_{eff} = 3.58 μ_B for free Pr^{3+} ion [30, 31]. The electronic structure of $PrCoO_3$ shows a strong hybridization of the Pr 4*f* states with the O 2*p* and Co 3*d* valence electronic states with Co^{3+} in the IS state at T = 300 K. Below T = 300 K, an increase of the Co^{3+} LS state is observed suggesting a first Co^{3+} IS / Co^{3+} LS transition [32]. A LS-LS / HS-IS transition model based on specific heat measurements and spin entropy calculations was successfully applied to described the second spin state transition at ~ 600 K [33]. The crystal-field splitting of the Pr^{3+} *4f* multiplet as well as the Co ions in the higher spin state behaving as scattering centers for phonons adds to the reduction of the phonon thermal conductivity [34].

Transition metal nitrides show high chemical stability, resistance to corrosion and good mechanical properties [35], especially high hardness. The hardness of the solid solutions of $Cr_{1-x}Ti_xN$ strongly depends on the chemical composition. It increases with increasing Ti concentration. This is due to the growth of larger grains which leads to a decrease in electrical resistivity [36]. Transition metal nitrides exhibit relatively low electrical resistivities associated with a large Seebeck coefficient in case of CrN. Thus, CrN can be considered as a promising thermoelectric material [37]. CrN is the only nitride that shows an antiferromagnetic-paramagnetic transition with a Neel temperature T_N ~ 273 K and a magnetic moment of 2.4 μ_B [38-40]. Below the magnetic ordering temperature T_N, the crystal structure transforms from cubic to orthorhombic. This change is due to the small distortion of the angle in the cubic structure [40]. The magnetic behavior of CrN is more complex as to the competition between the super-exchange (AFM) and double-exchange (FM) mechanism [41].

All the above-mentioned compounds could serve as potential thermoelectric materials. Hence, understanding the interrelation of their structural and physical properties is crucial in order to fine-tune and employ them in thermoelectric applications.

2. Thermoelectric oxide modules (TOMs)

A thermoelectric module consists of a large number of *p*- and *n*-type thermoelectric (TE) legs connected electrically in series and thermally in parallel. These legs are sandwiched between two ceramic plates with high thermal but low electrical conductivity. In this work, the TE legs were made of oxide materials. No real thermoelectric converters (multileg) were prepared, but a series of four leg perovskite thermoelectric oxide modules (TOMs) were tested for their ability to convert solar heat directly into electrical energy. The influence of the leg length, the emissivity of the absorber plate (graphite or SiC coating), and the heat flux on the maximum output power and the conversion efficiency was investigated. Furthermore, a solar thermoelectric cavity converter was constructed based on heat transfer and heat loss analysis. The aim of this converter is to concentrate simulated solar radiation and thereby improve the conversion efficiency.

2.1. Experimental part

2.1.1. Assembly of the thermoelectric oxide modules

A series of four-leg thermoelectric oxide modules were constructed combining two *p*- and two *n*-type legs. The thermoelectric legs had a surface area varying between 4 mm x 4 mm and 5.5 mm x 5.5 mm and a length (height) between 4 mm and 10 mm. $CaMn_{0.98}Nb_{0.02}O_3$ and $GdCo_{0.95}Ni_{0.05}O_3$ were used as *n*-type and *p*-type material, respectively. Eventually, the *p*-type material was changed for $La_{1.98}Sr_{0.02}CuO_4$, because of the better compatibility factor with the *n*-type material which improves the maximum output power of the TOMs. The thermoelements were connected electrically in series and thermally in parallel and placed between two thin Al_2O_3 absorber plates. The plates had a surface area between 25 mm x 25 mm and 30 mm x 30 mm and were 0.25 mm and 0.5 mm thick. They served as the electrically insulating and heat conducting substrate for both the cold and the hot side of the module.

Different electric contact, soldering and joining materials were tested in wetting experiments. Electrical contacts consisted of a mixture of Ag and CuO powders (2 wt% CuO for *n*-type, 0.5 wt% CuO for *p*-type). For this purpose, mixtures of Ag with 0.5 – 2 % CuO were pressed into disc-shaped pellets and annealed at T = 1193 K for several hours. After the thermal treatment, the Ag / CuO discs were further pressed by using a hydraulic press and polished to obtain the final metal foil with an approximate thickness of 150 µm. The foil was used to establish the electrical contacts between the ceramic legs and the Al_2O_3 substrates. Pellets of thermoelectric materials were covered with the electrical contact material and annealed in air up to 1243 K with a dwelling time of ten minutes. Finally, the thermoelectric legs were electrically connected in series by silver paste. The cross-section of the Al_2O_3 - Ag/CuO - *p*- and *n*-type leg joint was studied with a Hitachi S-4800 scanning electron microscope (SEM) in order to examine in detail the quality of the bonding.

2.1.2. Test set-up for the electrical and power measurements

A test set-up for the electrical and power measurements was mounted as shown in Fig. 1. The testing apparatus consists of: 1) a pressure device to control the pressure on the top side of the module and the heat transfer from the heater to the module, 2) a high accuracy control set-up to adjust the interfacial area between the heat source and the TOM surface, 3) a controllable electric heating plate to heat the upper side of the TOM and 4) a copper block cooling part with circulating cold water to cool the bottom side of the TOM. The pressure load on the module during the test was between 2 to 8 N cm^{-2}.

The output power at different loads was measured using automated parallel switching of four resistances by means of low-resistance relays. This configuration allows to provide 10 highly

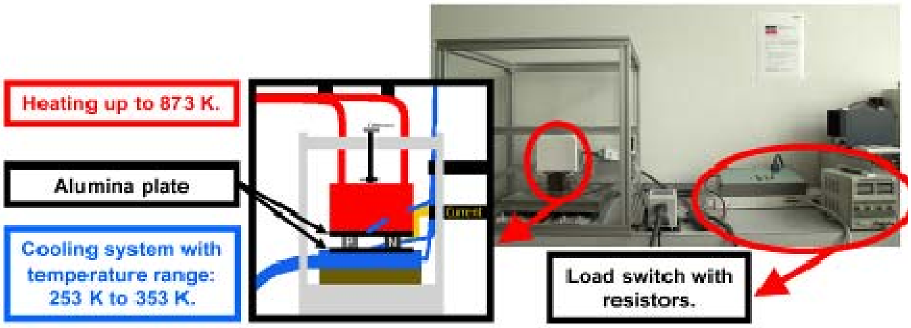

Fig. 1: Configuration of the testing apparatus for the electrical and power measurements.

precise loads (R_{load}). The voltage measurement in open circuit mode (V_{OC}) and at load resistances was realized by a precise digital multimeter (DMM). The measurement was monitored and recorded by a LABVIEW applet running on a desktop computer. The internal resistance R_{in} was calculated using the relation:

$$R_{in} = R_{load} \, [(V_{OC} - V_{load}) / V_{load}]. \tag{1}$$

The maximum output power (P_{max}) for various loads related to different load voltages was calculated by using the general relation:

$$P_{max} = V_{OC}^2 / [4 \, R_{load} \, ((V_{OC} - V_{load})/V_{load})]. \tag{2}$$

2.1.3. Heat transfer through the TOMs and temperature monitoring

Detailed information about the temperature distribution along the legs (temperature gradient) of the module was obtained by measuring the module's surface reflectance with a micro-IR camera (Jade III for microthermographic measurements from Cedip Infrared Systems, Fig. 2a). The InSb detector array of the camera has a resolution of 240 x 320 pixels and is sensitive to infrared radiation with wavelengths in the range of 3.6 - 5.0 µm. Dynamic measurements were performed with a frame rate of 10 Hz for the defined temperature gradient. A graphite spray was used to homogenize the surface emissivity of the samples. The data were evaluated using the IR-camera software.

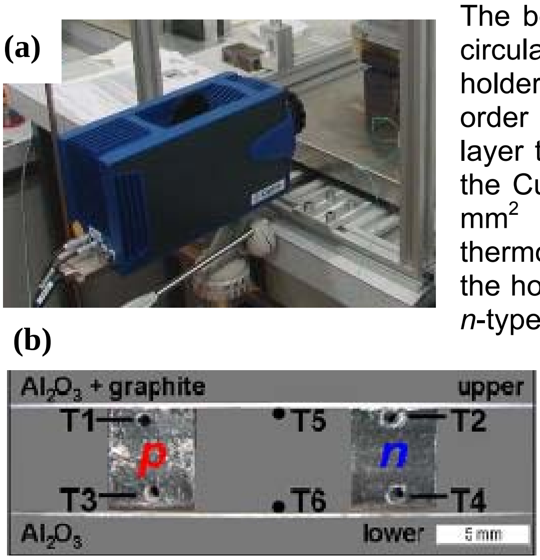

Fig. 2: (a) The micro-IR camera (f = 50 mm and a 10 mm extension ring) for temperature profile measurement. (b) Positions of the drilled holes for the 0.5 mm thick K-type thermocouples in a cross-sectional profile of the 5mm TOM.

The bottom side of the TOMs was cooled by cold water circulating in a Cu block. TOMs were fixed to the Al-holder using a thermally conductive paste (DuPont^{TM}) in order to increase the heat transfer from the cold Al_2O_3 layer to the Al-holder. The Al-holder itself was placed on the Cu block cooling unit with a surface area of 50 x 50 mm^2 (Fig. 3b). A series of 0.5 mm thick K – type thermocouples was used to measure the temperature on the hot and cold side of the TOM as well as in the *p*- and *n*-type legs. One thermocouple was attached to the hot and cold Al_2O_3 absorber layer, respectively, and two to each TE leg by means of drilled holes with 0.6 mm in diameter (Fig. 2b).

The temperature gradient along the TE legs was measured with thermocouples. The connection of the thermocouples was ensured by pressure contact and their position in the module is shown in Fig. 2a. K-type thermocouples were placed directly between the heating plate and the Al_2O_3 layer on the hot side of the module and between the Cu cooling block and the Al_2O_3 layer on the cold side of the module, respectively. Additional thermocouples were used to control the temperature of the heat source (in the case of a controllable heating plate) and the cooling water.

2.1.4. High-Flux Solar Simulator (HFSS)

A High-Flux Solar Simulator was used as heat source (Fig. 3a) [41]. A water-cooled, high-pressure argon arc lamp enclosed in a quartz shelter produces radiation in the visible, infrared and ultraviolet region of the spectrum. The power flux intensity and the temperature can be adjusted by varying the position of the target along the axis of the focusing mirrors or by changing the electrical input power at the arc electrodes. With the HFSS, flux intensities above 500 W cm^{-2} and temperatures exceeding 3000 K can be reached. The input heat fluxes (0 – 14.4 W cm^{-2}) were measured by a water cooled Thermogage Circular Foil Heat Flux Transducer TG1000-1 (Vatell Corporation) with a calibration range of 0 – 179 W cm^{-2}, a sensor sensitivity of 0.084 mV W^{-1} cm^{-2} and a sensor emissivity of 0.97.

Typical measurement runs started by applying different heat fluxes until temperatures at the TOM showed steady state behavior. Simultaneously, the voltages in the open circuit mode, the load resistances and the temperatures on the hot and cold side of the TOMs and the Al_2O_3 substrates were recorded.

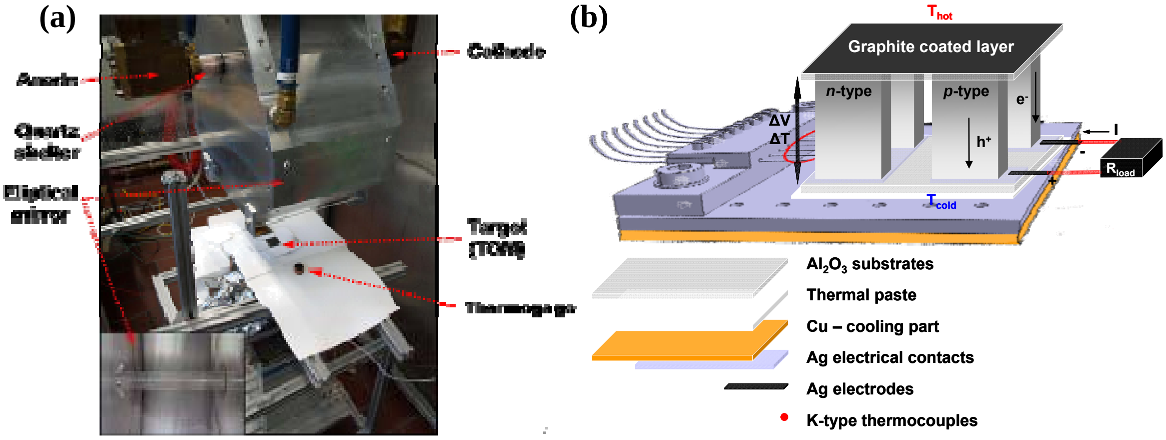

Fig. 3: (a) The High-Flux Solar Simulator at the ETH. An elliptical mirror redirects the radiant power of the enclosed argon arc lamp onto the target (TOM). (b) Sketch of a TOM testing unit mounted on the Al-holder for the thermocouples and the Cu-cooling part by thermal paste. The hot Al_2O_3 substrate of the four - leg TOM is coated by a graphite layer.

2.1.5. Solar thermoelectric cavity converter

A solar cavity-receiver packed with an array of thermoelectric oxide modules to convert concentrated solar radiation into electrical energy was designed, fabricated and tested (Fig. 4). The function of the cavity design is to capture the concentrated solar radiation efficiently and to reduce losses due to reradiation of the absorber plates. The thermoelectric oxide modules were tested at the High-Flux Solar Simulator at the ETH. TOMs were measured individually as well as serially connected at different radiant intensities in terms of temperature distribution in the cavity, open-circuit voltage and power output at different external loads.

2.2. Results

$La_{1.98}Sr_{0.02}CuO_4$ and $CaMn_{0.98}Nb_{0.02}O_3$ with thermal conductivities of 2.5 W m^{-1} K^{-1} and 3 W m^{-1} K^{-1} above 300 K, respectively, were used as *p*- and *n*-type materials for the TOMs. The materials were hydrostatically pressed into pellets and showed 90% of the theoretical density without any crack formation due to the uniformly applied pressure. High density of the TE legs is the requirement for the production of mechanical stable TE modules. Thus, it is essential to find materials that combine a low thermal conductivity with a good mechanical stability.

In this study, we applied optimum materials with similar thermoelectric properties in order to build an efficient TOM. At T = 300 K both the *p*- and *n*-type legs show metallic behavior with a similar electrical resistivity (ρ_p = 24 mΩ cm and ρ_n = 20 mΩ cm, respectively) and exhibit a large thermopower (S_p = +200 μV K^{-1} and S_n = -160 μV K^{-1}, respectively).

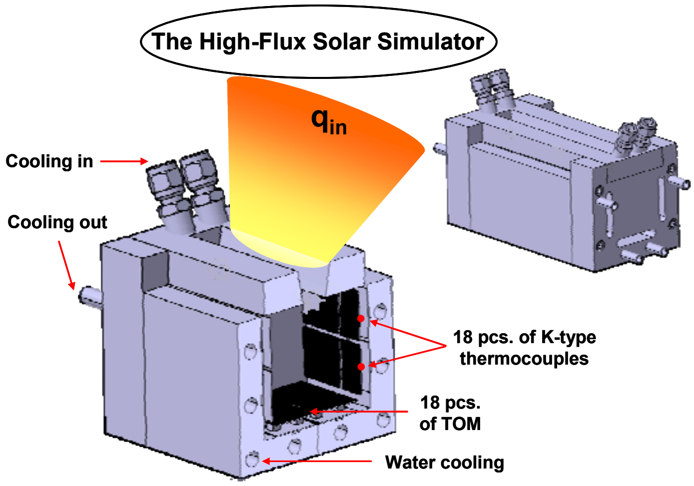

Fig. 4: The solar thermoelectric cavity converter with 18 graphite-coated TOMs and K-type thermocouples for temperature monitoring.

Similar thermoelectric properties of the materials are a prerequisite for good conversion efficiencies of TE modules as previously described by G. Snyder et al. [42]. The compatibility factor *s*, defined as $s = [(1+ZT)^{-1/2}-1]/ST$, is used to assess the similarity of thermoelectric properties of different materials. While other thermoelectric parameters can change dramatically with temperature, the compatibility factor should be mainly temperature-independent in order to achieve maximum efficiency [42]. The more similar the compatibility factors of two materials are the higher will be the maximum efficiency of the thermoelectric module. The compatibility factors of the above-mentioned materials are perfectly matching around T = 425 K. However, with increasing temperature the ratio of the compatibility factors becomes 1.3 at T = 500 K and 2.3 at T = 800 K. Thus, the efficiency of the four-leg modules decreases at higher temperatures.

In the temperature range of 300 – 450 K, the Figure of Merit *ZT* of the *p*-type material is higher than that of the *n*-type material due to its higher Seebeck coefficient. At T > 400 K, the *ZT* value of the *p*-type leg decreases as the Seebeck coefficient decreases (*S* ~ 130 μV K^{-1} at 800 K) while the *ZT* value of the *n*-type leg still increases due to *S* ~ -240 μV K^{-1}, resulting in ZT ~ 0.08 at T = 800 K.

The maximum temperature that can be applied when using a graphite-coated Al_2O_3 absorber plate is limited to T ~ 910 K where the graphite starts to sublimate. Sublimation would results in a decrease in temperature difference between the hot and cold side of the module as well as in a decrease in output power and conversion efficiency (Fig. 5). This is caused by the lower absorptivity of the Al_2O_3 absorber plate when the graphite coating vanishes. By increasing the heat flux, the temperature on the hot side of the module (*T5*) increases as expected. All results are summarized in Table I. At the same heat flux, temperatures on the hot side of the *p*- and *n*-type TE legs (*T1*, *T2*) are comparable which means that the interconnection quality between the hot Al_2O_3 layer and the TE legs is equivalent. Inducing absolute temperatures > 400 K, temperatures on the cold side of the module are lower in the *p*-type leg (*T3*) than in the *n*-type leg (*T4*) due to a lower thermal conductivity of the *p*-type material.

On the cold side of the Al_2O_3 absorber plate (*T6*), temperatures are not equal which can be explained by a not sufficiently tight contact between the module and the Al-holder and deficiencies of the thermal paste. The difference amounts up to 140 K for the 4 mm TOM 1 and the 5 mm TOM 4. As the 5 mm TOM 4 was coated with SiC (*ε* ~ 0.7; total spectrum measured) [43] the lower temperature gradient compared to the graphite-coated 5 mm TOM 1 (*ε* ~ 0.95 – 0.97; total spectrum measured) [43] was expectable. The temperature gradient along the TE legs is almost linear. Above T = 400 K, temperature profiles of the *p*-type legs show lower values than of the *n*-type legs due to a higher thermal conductivity at this temperature. The temperature difference between the uncoated and the graphite-coated Al_2O_3 absorber plate on the hot side (*T5*) is ~ 160 K for a heat flux of 9.5 W cm^{-2}. This results from improved heat absorption due to a higher emissivity of the coated surface. Additionally, insufficient cooling leads to an increase of 7 K on the cold side of the module (*T6*).

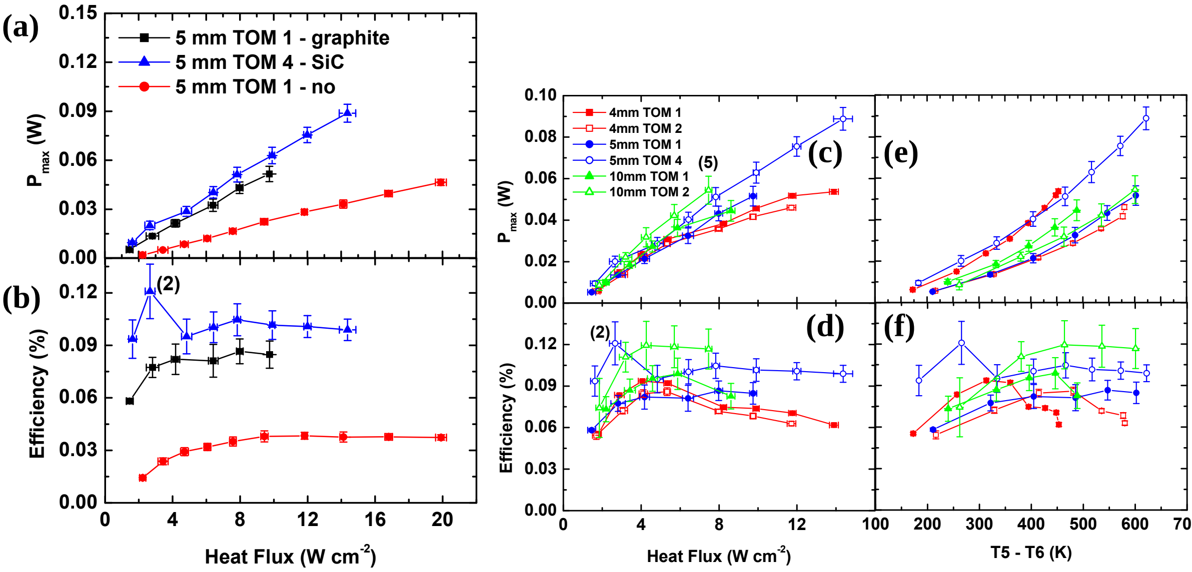

Fig. 5: (a) Maximum output power and (b) conversion efficiency as function of heat flux of 5 mm TOM 1 and 5 mm TOM 4. Maximum output power and conversion efficiency (c, d) as a function of heat flux and (e, f) as a function of the temperature difference between hot plate and cold plate, respectively.

Based on the voltage measurements in open-circuit mode (V_{oc}) and at load resistances, the maximum output power (P_{max}) was calculated considering the load resistance equal to the internal resistance [44]. P_{max} for 5 mm coated and uncoated TOMs is plotted in Fig. 5a. For the 5 mm TOM 1, P_{max} is higher for the graphite coated than for the uncoated module. At the same heat flux of ~ 9.5 W cm^{-2}, the temperature difference between *T5* and *T6* amounted to 602 K and 448 K for the graphite coated and the uncoated 5 mm TOM 1, respectively. Accordingly, an open circuit voltage V_{OC} of 44.6 mV (graphite-coated) and 31.7 mV (uncoated) was measured resulting in an output power P_{max} of 51.6 mW and 22.6 mW, respectively. For the 5 mm SiC-coated TOM 4, V_{OC} = 38.3 mV, $T5 - T6$ = 507 K and P_{max} = 60.6 mW at a heat flux of ~ 9.5 W cm^{-2}. Despite the lower emissivity of SiC compared to graphite the 5 mm TOM 4 has a higher maximum output power P_{max} even though the open circuit-voltage V_{OC} is smaller. As the same *p*- and *n*-type materials are used for all the TOMs, this finding might only be due to small manufacturing deviations which could affect the contact resistances.

Knowing the input heat flux measured by the Thermogage, and the open-circuit voltage V_{oc} measured by a test unit with a data logger, we can calculate the conversion efficiency η, defined by:

$$\eta = \frac{V_{OC}^2}{4R_{load}\left(\frac{V_{OC}-V_{load}}{V_{load}}\right)Q_{in}}, \qquad (3)$$

where V_{load} is the voltage at load resistance, R_{load} is the load resistance, and Q_{in} is the input heat flux on the surface of the Al_2O_3 absorber plate. Conversion efficiencies against heat flux for 5 mm TOMs are presented in Fig. 5b. The conversion efficiencies of the graphite-coated 5 mm TOM 1 and the SiC-coated TOM 4 are higher than the efficiency of the uncoated 5 mm TOM 1 which is in agreement with the P_{max} results. As for the 5 mm TOM 4, the discordant value of η (2nd point of the blue curve in Fig. 5b) was caused by a combination of radiation fluctuation (horizontal error bars) and the instability of V_{load} (vertical error bars). Fig. 5c-f summarize the data for P_{max} and η vs. heat flux and $T5 - T6$ for 4, 5 and 10 mm TOMs coated with graphite (5 mm TOM 4 coated with SiC). Depending on the temperature difference *T5 – T6*, the maximum output power P_{max} increases exponentially and the maximum value of 54.4 mW was achieved for a leg length of 10 mm (5th point in Fig. 5e).

Depending on the heat flux, the maximum output power of 88.8 mW was obtained for the 5 mm TOM 4 at a heat flux of 14.4 W cm^{-2} and a temperature difference of *T5 – T6* = 622 K. Theoretically, the highest P_{max} value would be expected for a 10 mm TOM. However, sublimation of the graphite coating at high temperatures (caused by heat fluxes exceeding 7.5 W cm^{-2}) leads to lower values.

Table I: Summary of the properties of four – leg TOMs.

	ΔT [K]	$q_{in,\ max}$ [W cm^{-2}]	$V_{OC,\ max}$ [mV]	η [%]	P_{max} [mW]	$q_{in,\ opt}$ [W cm^{-2}]	η_{max} [%]	A/l [mm]	R_{int} [Ω]	R_{mater} [Ω]	R_{cont} [Ω]	MQF1 [%]	MQF2 [%]
4 mm TOM 1	453	13.90	42.9	0.043	53.7	4.06	0.065	5.06	0.86	0.27	0.59	23	31
4 mm TOM 2	580	11.72	39.4	0.044	46.1	5.33	0.060	5.06	0.84	0.26	0.58	11	31
5 mm TOM 1	602	9.75	44.5	0.059	51.6	7.98	0.060	4.05	0.96	0.32	0.64	14	33
5 mm TOM 4 *	622	14.37	46.4	0.069	88.8	7.83	0.073	4.05	0.61	0.32	0.29	23	52
10 mm TOM 1	489	8.61	45.3	0.058	44.5	5.87	0.069	2.03	1.15	0.66	0.49	38	57
10 mm TOM 2	601	7.46	52.4	0.081	54.4	4.26	0.082	2.03	1.26	0.65	0.61	31	52

$\Delta T = T5_{max} - T6_{max}$.

$T5_{max}$ and $T6_{max}$ are the maximum temperatures reached by applying maximum input heat flux $q_{in,\ max}$.

$V_{OC,\ max}$, η and P_{max} are the maximum open circuit voltage, efficiency and maximum output power reached by applying maximum input heat flux $q_{in,\ max}$.

$q_{in,\ opt}$ is the optimum input heat flux for reaching the maximum conversion efficiency η_{max}.

* Coated by SiC.

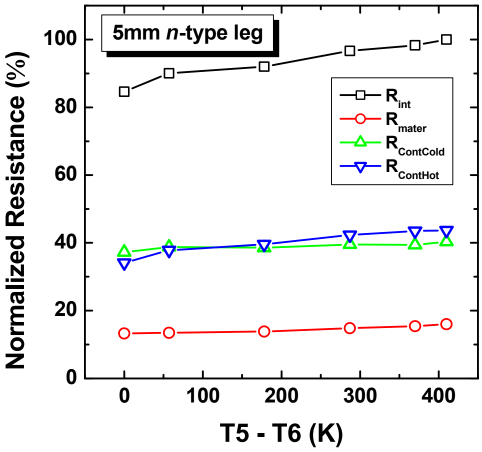

Fig. 6: (a) Contact resistance measurement configuration based on eqs. 5-7 and (b) normalized R_{int}, R_{mater}, $R_{contcold}$ and $R_{conthot}$ for 5 mm n-type TE leg.

The maximum conversion efficiency of 0.12 % was obtained for a TOM with 10 mm leg length and an Al_2O_3 absorber area of 25 x 25 mm^2 (Fig. 5d, f). Taking an absorber surface area equivalent to the area of the *p*- and *n*-type legs as a basis, the maximum conversion efficiency will reach ~ 1 %. The conversion efficiency is higher at higher heat fluxes resulting in higher temperature differences *T5 – T6* which improves the Carnot efficiency. However, at higher temperatures and higher heat fluxes the emissivity of the Al_2O_3 absorber plate increases with T^4. Thus, the conversion efficiency reaches an optimum value after which it decreases. The optimum conversion efficiency for 4 mm TOMs is around 4 W cm^{-2}, for 5 mm TOMs between 4 – 8 W cm^{-2} and for 10 mm TOMs around 6 W cm^{-2}.

The TOM's conversion efficiency does not only depend on the thermoelectric properties of the TE materials, the temperature differences across the TOMs, the overall geometry of the device (such as filling factors etc.), but also on the contact resistances. Ideally, the internal resistance R_{int} of the module is equal to the resistance of the thermoelectric oxide material R_{mater}. However, in real thermoelectric modules, the contribution of the contact resistance is not negligible and lowers their conversion efficiency remarkably. The internal resistances, contact resistances and material resistances of the TOMs were evaluated and are summarized in Table 1. The internal resistance increases with leg length because of the increase of the material resistance R_{mater}. The contact resistance varies in the range of 0.29 Ω < R_{cont} < 0.64 Ω depending on the manufacturing quality of TOMs.

For a more detailed analysis the internal resistance R_{int} and the contact resistances on the hot side $R_{conthot}$ and the cold side $R_{contcold}$ of 5 mm *n*-type TE legs were determined at several temperature differences varying from 0 K to 410 K. The data were normalized and is plotted in Fig. 6. The measurement shows that the contact resistances on both the cold and the hot side of the TOM make a significantly higher contribution to the internal resistance than the resistance of the thermoelectric oxide materials. Thus, it can be concluded that for better conversion efficiencies the quality of the contacts has to be improved e.g. by developing better contact materials.

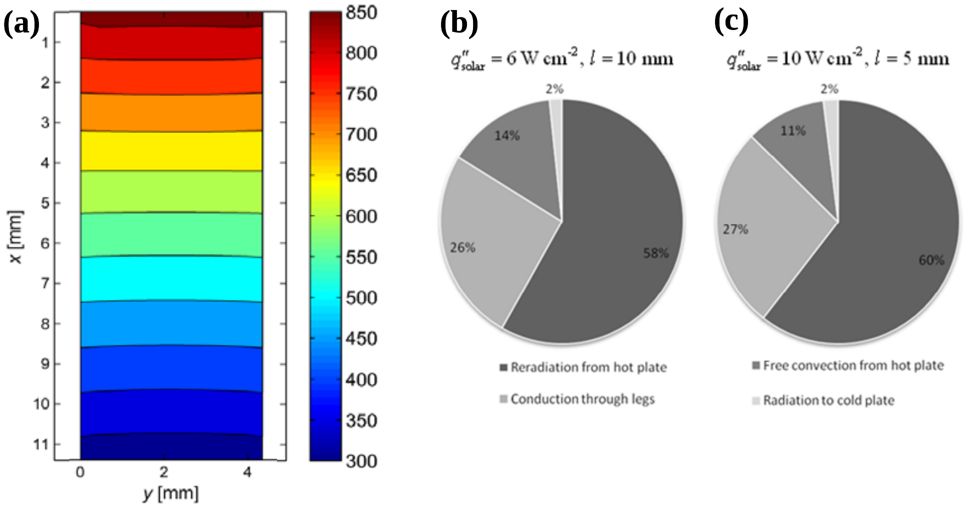

Fig. 7: (a) Temperature profile along the 10 mm length of p-type ($La_{1.98}Sr_{0.02}CuO_4$) leg at a heat flux of 6 W cm^{-2}. (b) Analysis of the heat transfer mode through a 10 mm TOM at a heat flux of 6 W cm^{-2} and (c) through a 5 mm TOM at a heat flux of 10 W cm^{-2}.

Interior radiation and heat conduction in the module were calculated by Clemens Suter, ETH, based on the thermoelectric properties of the *p*- and *n*-type materials and the absorber plate. The theoretical study was carried out under the boundary conditions of a fixed temperature on the cold side of the TOM, constant diffuse solar flux from the solar source, no local convection and open circuit voltage (j = 0, V = 0). Fig. 7a reveals that the temperature distribution along the *p*-type leg is linear. The analysis of the heat transfer through a 5 mm and 10 mm TOM is shown in Fig. 7b and c, respectively. The calculations indicate that only ~ 25 % of the heat input is conducted through the TOM, approximately 70 % is lost due to either radiation or free convection and about 2 % due to radiation to the Al_2O_3 absorber plate on the cold side of the TOM.

The conversion efficiency was significantly improved by irradiating 18 four-leg TOMs inside a cavity. The maximum output power of 1.4 W was obtained using a heat flux of ~ 100 W cm^{-2}.

3. Characterization methods - Experimental techniques

- The synthesis – Solid state reaction and soft chemistry route
- The structure and phase composition - X-ray powder diffraction (XRPD) using a Phillips X'Pert PRO MPD Θ-Θ
- The morphology - Scanning electron microscopy (SEM) and Transmission electron microscopy (TEM) using a Hitachi S-4800 and Philips CM 30
- The O/N content - Hot gas extraction (HGE) using a LECO TC500 analyzer
- The thermal stability and oxygen content – Thermogravimetric analysis (TGA) / Differential thermal analysis (DTA) / Differential scanning calorimetry (DSC) measurements using a Netzsch STA 409 CD thermobalance and Netzsch DSC 404 C Pegasus
- The low temperature (2 K < T < 400 K) electrical and thermal transport using a Thermal transport option (TTO) for Physical Property Measurement System (PPMS)

- The high temperature (310 K < T < 1273 K) electrical and thermal transport using the RZ2001i Ozawa Science, Japan measurement system and Netzsch Laser flash apparatus (LFA)
- The low temperature (4 K < T < 400 K) magnetic susceptibility and magnetic moment measurements using a Vibrating sample magnetometer (VSM) adaptor for the Physical Property Measurement System (PPMS)
- The low temperature (2 K < T < 400 K) heat capacity measurements K using a ^{3}He Heat Capacity puck for PPMS

4. Studies on new ceramic thermoelectric materials

4.1. $Sr_{1-x}Na_xRuO_3$ (x = 0 – 0.19)

The morphology of the $Sr_{1-x}Na_xRuO_3$ (x = 0 – 0.19) samples was determined by Scanning Electron Microscopy (SEM) and is shown in Fig. 8. The ceramic samples are composed of particles with average sizes between 50 – 1500 nm. We found that samples with x = 0.09 and x = 0.16 are made up of large crystallites while the samples with x = 0.0 and especially with x = 0.19 consist of grains with a dispersion down to ~ 50 nm. In general, smaller grains improve the material's electrical conductivity. Thus, a lower resistivity for samples with x = 0.0 and x = 0.19 compared to samples with x = 0.09 and x = 0.16 can be expected. In fact, the lowest resistivity is observed for the sample with x = 0.19 (Fig. 9). This is likely due to the favorable morphology of the ceramic sample containing mostly fine grains which embed a small amount of large crystallites (Fig. 8e). These crystallites where surveyed by electron microprobe and an unexpected high Na concentration was measured (Fig. 8f). Energy dispersive X-ray (EDX) analysis identified the needle-shaped impurity phase to be the insulating hexagonal perovskite Sr_3NaRuO_6 [45].

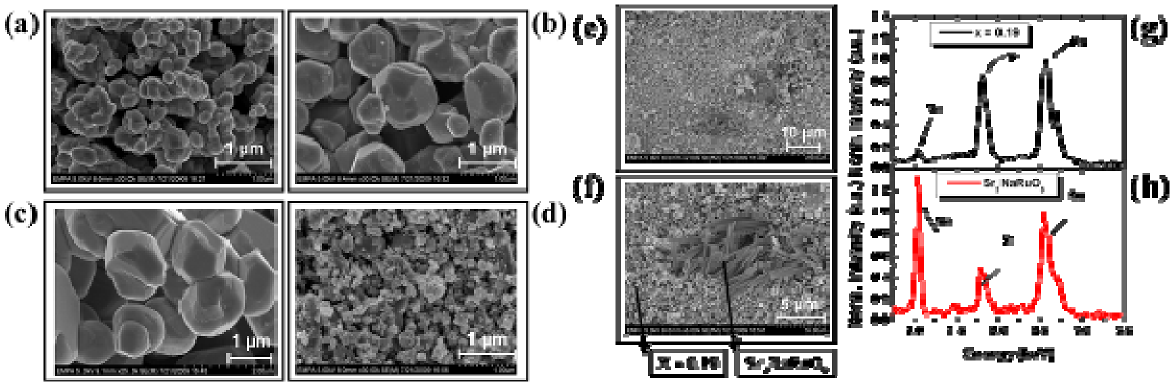

Fig. 8: SEM pictures of the samples with (a) x = 0.0, (b) x = 0.09, (c) x = 0.16, (d) x = 0.19. SEM pictures of the sample (e, f) x = 0.19 and EDX spectra of the (g) x = 0.19 and the (h) impurity phase of Sr_3NaRuO_6*.*

All the solid solutions of the $Sr_{1-x}Na_xRuO_3$ system have orthorhombic crystal structure and belong to the *Pbnm* space group. The ratio of the cell parameters $a > c/\sqrt{2} > b$ is valid for all Na-doped compounds. The lattice parameters are linearly decreasing with increasing Na substitution on the A-site which is due to the lower ionic radius of Na ($r_{Na+} < r_{Sr2+}$). Consequently, all the samples of $Sr_{1-x}Na_xRuO_3$ (x = 0.0 - 0.19) have a Goldschmidt tolerance factor $t < 1$ which decreases with increasing x while a small orthorhombic distortion remains constant at ~ 0.43 ± 0.04 %. The Ru – O bond length slightly decreases with increasing Na content and the valence bond angle Ru – O – Ru varies between 163 – 164 °. The valence bond angle differs from the ideal cubic angle because of the cooperative rotation of the RuO_6 octahedra in $SrRuO_3$.

The temperature dependence of the thermal and electrical properties is shown in Fig. 9. The total thermal conductivity in this temperature range increases with increasing temperature. At room temperature, values vary between 1.5 and 2.8 W m^{-1} K^{-1}. The total thermal conductivity is composed of an electronic and a phononic part according to $\kappa_{total} = \kappa_{el} + \kappa_{ph}$, The electronic part κ_{el} can be roughly estimated using the Wiedemann - Franz law, $\kappa_{el} = L_0 \sigma T$, where L_0 = 2.443 10^{-8} W S^{-1} K^{-2} is the Lorenz number for free electron gas, σ is the electrical conductivity, and T is the absolute temperature. From this the phononic part can be. The phonon thermal conductivity κ_{ph}, varying between 1.3 and 1.7 W m^{-1} K^{-1} at 300 K, changes with temperature and despite the low compactness of the samples (~ 60 %) and the glass-like behavior without typical low temperature enhancement, κ_{ph} exhibits a small change below T_C. This indicates that regardless a strong scattering of phonons on other phonons, grain boundaries and defects there could be a significant coupling between phonons and spin excitations. Consequently, the magnetic transition at T_C is not purely a 2nd order transition but also involves, at least to a small extend, the lattice degree of freedom by spin – lattice coupling.

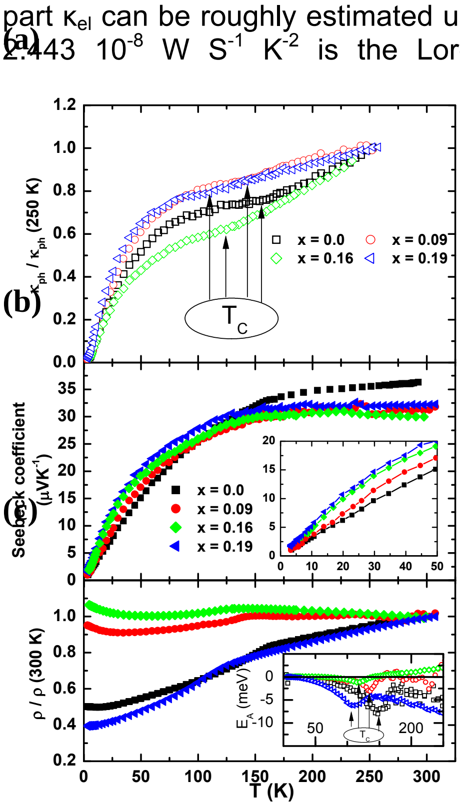

Fig. 9: (a) Temperature dependence of the phonon part of the thermal conductivity normalized to T = 250 K, (b) Seebeck coefficient and (c) electrical resistivity normalized to T = 300 K for the $Sr_{1-x}Na_xRuO_3$ (x = 0.0-0.19) system.

The temperature dependence of the Seebeck coefficient and the electrical resistivity is plotted in Fig. 9b and c, respectively. All the samples show metallic behavior with $d\rho / dT > 0$. The resistivity values at 300 K vary between 0.75 to 16.3 mΩcm and predominantly depend on the morphology and microstructure of the ceramic sample. As expected, the sample with x = 0.19 exhibits the best metallicity which is likely due to the small grain size.

The Seebeck coefficient S for all samples, shown in Fig. 9b, is positive in the whole temperature range indicating the dominant role of holes in the electronic conduction mechanism. The high temperature Seebeck coefficients approach constant values between 31 and 36 μV K^{-1} at 300 K. The change of the slope at T_C is likely associated with the change of spin entropy which may contribute to the Seebeck coefficient at high temperatures [47]. The almost linear temperature dependence of the Seebeck coefficient at low temperatures (inset of Fig. 9b) reflects the metallicity of all the samples. The high S / T slope *is in* agreement with a high Sommerfeld coefficient γ (varying between 30.9 mJ mol^{-1} K^{-2} (x = 0.0) to 43 mJ mol^{-1} K^{-2} (x = 0.19)) according to Behnia et al. who found that the S / T ratio and γ increase simultaneously with increasing x [48].

4.2. $CrO_{0.09(3)}N_{0.90(7)}$

It was determined that CrN has a cubic crystal structure with *Fm-3m* space group and a lattice parameter a = 4.1506(2) Å. The refinement of the XRD data is plotted in the left diagram of Fig. 10. The inset shows the unit cell of the perovskite-type crystal structure of Cr – O – N. The atomic percent ratio of 0.09 for oxygen replacing nitrogen was measured by hot gas extraction resulting in the nominal composition $CrO_{0.09(3)}N_{0.90(7)}$. This composition was considered for the Rietveld refinement of the crystal structure. The TGA / DTA measurement was performed in order to estimate the temperature stability of the sample. The observed mass increase above T ~ 700 K was due to oxidation of $CrO_{0.09(3)}N_{0.90(7)}$. This decomposition point is much better than that of conventional thermoelectric modules based on Bi_2Te_3 which operate far below 700 K because of their low temperature stability. Figures 10 a-d show TEM diffractograms, conventional images and high resolution images of the Cr – O - N sample. Fig. 10a represents the diffraction pattern and the indexing which is in agreement with the atomic model obtained by Rietveld refinement. The particle size is ranging from 30 to 150 nm and particles mainly have polygonal shapes (see detailed size and morphology of the Cr – O - N particles in Fig. 10b and c). Similar particle sizes between 10 and 50 nm were also found by Inumaru et al. [50]. Due to the small particle size the electrical resistivity is reduced to 2.8 mΩcm at room temperature (see below). The high resolution image of one particle shown in Fig. 10d corresponds to the zone axis and confirms the good crystallinity of the sample [36, 38, 39, 49-55].

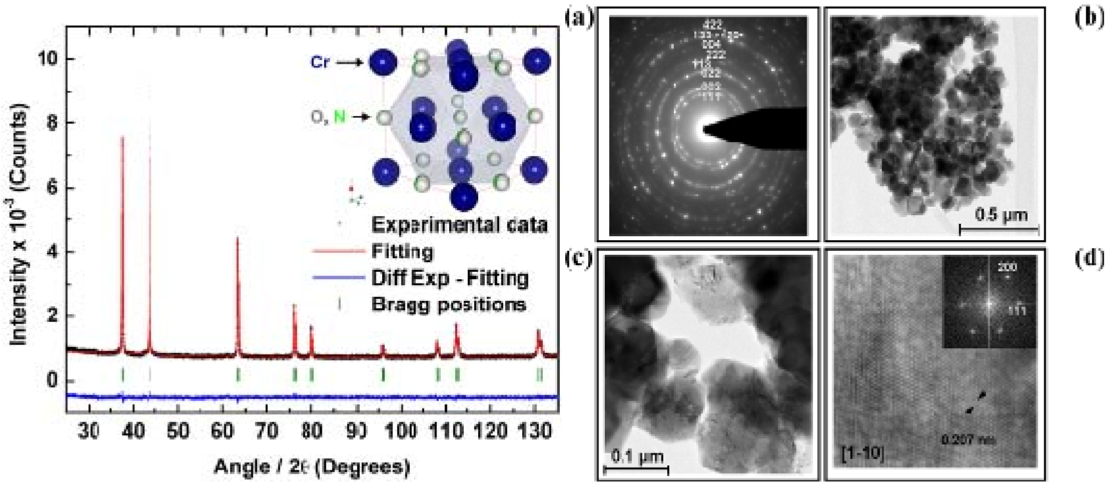

Fig. 10: (Left diagram) Rietveld refinement of the X-ray powder diffraction data for $CrO_{0.09(3)}N_{0.90(7)}$. Space group: Fm-3m. The observed intensities, calculated profile, difference curve and Bragg positions are shown. The inset shows the picture of the cubic perovskite-type crystal structure of $CrO_{0.09(3)}N_{0.90(7)}$. (Right diagram) (a) Diffraction pattern and indexing which is in agreement with the atomic model obtained by Rietveld refinement, (b, c) detail of the size and morphology of the Cr – O - N particles and (d) high resolution image of one particle which corresponds to the [1-10] zone axis and confirms the good crystallinity of the sample.

The temperature dependence of the electrical resistivity and Seebeck coefficient, *S,* between 3 K < T < 850 K are plotted in Fig. 11 a-b. The inset of Fig. 11a shows the hysteresis of the electrical resistivity measurement during the cooling and heating. This hysteresis was reported by several research groups [38] and is associated with a structural phase transition. The low electrical resistivity of ~ 2.8 mΩcm at T = 300 K reflects the metallic nature of the compound. Such a low value was also measured for $Cr_{0.9}V_{0.1}N$ by Quintela et al. [37]. They reported the systematical gradual suppressing of the electrical resistivity by increasing the vanadium content in the CrN matrix.

The Seebeck coefficient of the sample is negative indicating that the main charge carriers are electrons. It is linearly decreasing with temperature which is typical for metallic compounds. Between 255 K and 265 K, *S* drops from -56 µV K^{-1} to -46 µV K^{-} and at T = 300 K S = -48 µV K^{-1}. However, the Seebeck coefficient of $CrO_{0.09(3)}N_{0.90(7)}$ is smaller compared with $Cr_{0.9}V_{0.1}N$ (*S* = -83 µV K^{-1} at T = 300 K) [37]. The low electrical resistivity and |*S*| > 100 µV K^{-1} result in a power factor *PF*, defined as PF = S^2 / ρ, of ~ 1.7 10^{-4} W K^{-2} m^{-1} at T = 590 K. Due to much higher Seebeck coefficients, higher PF values of ~ 2.0 10^{-4} W K^{-2} m^{-1} and 3.0 10^{-4} W K^{-2} m^{-1} are reported for $Cr_{0.95}V_{0.05}N$ and $Cr_{0.9}V_{0.1}N$, respectively [37].

The bulk sample density is 60 % of the theoretical density. Total thermal conductivity composed of an electronic and phononic part $\kappa_{total} = \kappa_{el} + \kappa_{ph}$ is plotted in Fig. 11c. The thermal conductivity increases with increasing temperature indicating metallic behavior and decreases between 255 K < T < 265 K by about 35 % from 4.2 $Wm^{-1}K^{-1}$ to 2.7 $Wm^{-1}K^{-1}$. Since κ_{ph} makes the main contribution to the total thermal conductivity κ_{total} of $CrO_{0.09(3)}N_{0.90(7)}$, the phononic part has to be reduced in order to be make the material interesting for possible future thermoelectric applications.

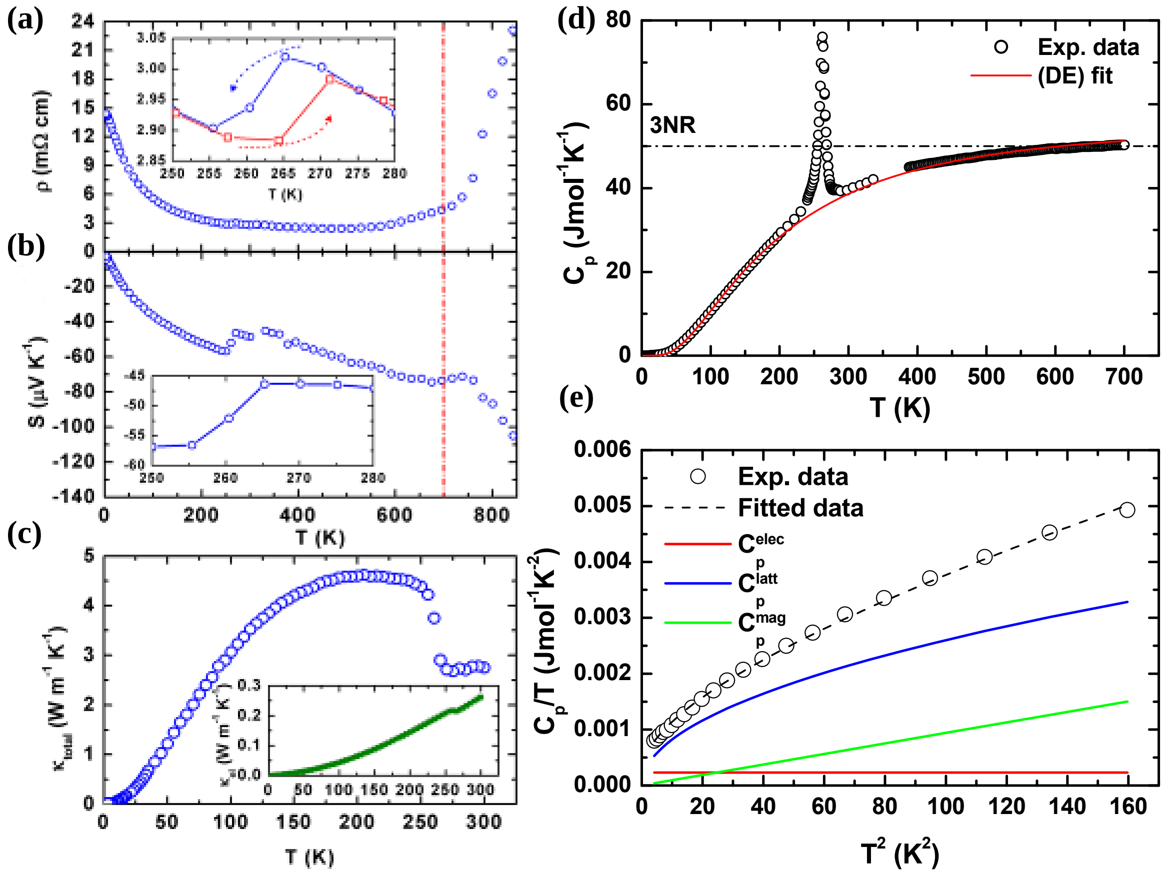

Fig. 11: (a) Temperature dependence of the electrical resistivity with the zoom around T_C during the cooling and heating, (b) Seebeck coefficient and (c) thermal conductivity with the inset showing the electronic contribution (κ_{el}) to total thermal conductivity of $CrO_{0.09(3)}N_{0.90(7)}$.(d) Temperature dependence of the heat capacity (C_p) of $CrO_{0.09(3)}N_{0.90(7)}$ fitted by involving the Debye-Einstein model. (e) Low temperature region of the heat capacity (C_p) with the fitting function, lattice, electronic and magnetic contributions to heat capacity of $CrO_{0.09(3)}N_{0.90(7)}$.

Fig. 11d shows the temperature dependence of the heat capacity C_p along with a fitting curve. The significant peak at T = 262 K indicates the paramagnetic (PM)-antiferromagnetic (AFM) and the structural transition and this temperature range (220 K < T < 306 K) was not included in the fitting process. Curve fitting was based on the modified Debye-Einstein (DE) model. The

DE model contains one triply degenerated Debye mode described by three acoustic branches and three Einstein modes with nine optical branches:

$$C_p = R\left(\left(\frac{3}{x_D}\right)^3 \int_0^{x_D} \frac{x^4 e^x}{\left(e^x - 1\right)^2} dx + \sum_{i-1}^{3} \frac{w_{Ei} x_{Ei} e^{x_{Ei}}}{\left(e^{x_{Ei}} - 1\right)^2}\right) + TV\alpha^2\beta^{-1} \text{ [26],}$$

where $x_D = \Theta_D / T$, $x_E = \Theta_{Ei} / T$ and w_{Ei} = 1, 5, 3 are the optical branches selected to obtain the best fitting. The last term represents the lattice dilatation, where α is the volume thermal expansion coefficient and β is the isothermal compressibility factor for the unit cell volume V = 21.531 10^{-6} m^3 measured at T = 300 K. As an approximation we used the data corresponding to CrN: α = 5.75 10^{-6} K^{-1} and β = 7 10^{-12} Pa^{-1}. The contribution of C_{dilat} to the total heat capacity is ~ 2.1 J mol^{-1} K^{-1} at T = 700 K. According to Dulong-Petit´s law, the limiting C_p at high temperatures (e.g. above 300 K) for a system containing r atoms per molecule is $C_p^{DP} = 3Rr$, where R is the universal gas constant. With this we obtain for the $CrO_{0.09(3)}N_{0.90(7)}$ system a limiting C_p of 49.9 J mol^{-1} K^{-1}. Experimentally, the heat capacity approaches a limit of C_p = 50.3 J mol^{-1} K^{-1} at T = 700 K. The resulting parameters for

$CrO_{0.09(3)}N_{0.90(7)}$ are: Θ_D = 663 K, Θ_{E1} = 287 K, Θ_{E2} = 568 K, Θ_{E3} = 1116 K (standard deviation $\lambda^2 < 0.25$).

In Fig. 11e C_p / T is plotted vs. T^2 in the low temperature region. The fitting curve is given by $C_p = \gamma T + \beta T^3 + \delta T^n$ and the individual terms are plotted in Fig.11e, too. The first term is the electronic part of the total heat capacity represented by the Sommerfield coefficient γ. The second term is the lattice (phonon) part represented by $\beta = \frac{12}{5} \cdot \frac{\pi^4 RN}{\Theta_D^3}$, where N is the number of atoms per mol and Θ_D is the Debye temperature. The last term δT^n represents the magnetic contribution of the spin waves to the total heat capacity. The Sommerfield coefficient γ and the Debye temperature were determined from the low temperature fitting resulting in γ = 0.23 mJ mol^{-1} K^{-1} and Θ_D = 745 K. The Debye temperature determined from the low temperature C_p data exceeds the Debye temperature derived from the high temperature data by 80 K. This finding might be attributed to the involvement of localized spins in the stiffness of the lattice. Thus, the magnetic contribution (δT^n) to the heat capacity dominates at low temperatures with a calculated coefficient δ = 0.26 mJ mol^{-1} K^{-3}. The fitting converged to n = 2 which is a typical value for an *A*-type antiferromagnetic structure. Integration of C_p / T yields the absolute entropy at standard conditions S_m^0 (300 K) = 33.78 J mol^{-1} K^{-1}.

4.3. $PrCo_{1-x}Ni_xO_3$ (x = 0 – 0.7)

All the $PrCo_{1-x}Ni_xO_{3\pm\delta}$ (0.0 < x < 0.62) phases have orthorhombic crystal structure with *Pbnm* space group. The refined lattice parameters increase with increasing Ni content. The ratio $a > c/\sqrt{2} > b$ is valid for all Ni-doped compounds. The Seebeck coefficient, thermal conductivity and electrical resistivity in the temperature range of 3.5 K < T < 300 K were measured on bar shaped pellets with theoretical densities of ~ 92 % for the sample with x = 0.62 and of ~ 65 % for all other samples. The temperature dependence of the electrical resistivity is plotted in Fig. 12a. The samples with 0.0 ≤ x ≤ 0.29 show insulating behavior with $d\rho / dT < 0$ whereas the samples with 0.49 ≤ x ≤ 0.62 show semiconducting to metallic behavior. The resistivity values at 300 K vary between 2.4 10^4 and 8.3 mΩcm. The activation energy E_a defined as $E_a = k_B \cdot d(\ln \rho) / d(1/T)$, derived from the Arrhenius law ($\rho(T) = \rho\infty \exp(E_a / k_B T)$), gives values of 560 meV, 400 meV, 270 meV and 430 meV for x = 0.07; 0.29, 0.49 and 0.62, respectively, at T = 300 K (inset of Fig. 12a). The activation energy of the samples with x = 0.07 and x = 0.29 shows nonlinear behavior in the temperature range of 5 K < T < 300 K. For the sample with x = 0.07 the activation energy reaches the maximum E_a = 550 meV at T = 115 K followed by the energy minimum at T = 230 K. The sample with x = 0.29 has an activation maximum at T = 280 K and in the temperature range of 120 K < T < 185 K the activation energy approaches a constant value E_a = 380 meV.

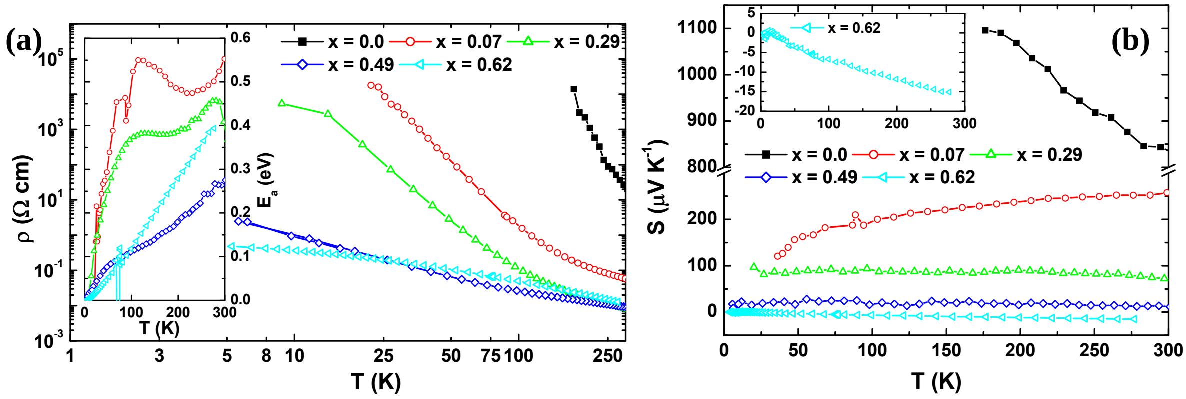

Fig. 12: (a) Temperature dependence of the electrical resistivity for PrCo$_{1-x}$Ni$_x$O$_{3\pm\delta}$ (0.0 < x < 0.62) with the inset of the activation energy defined as $E_a = k_B \cdot d(\ln\rho)/d(1/T)$. (b) Temperature dependence of the Seebeck coefficient; the inset shows the temperature dependence of the Seebeck coefficient of PrCo$_{0.38}$Ni$_{0.62}$O$_3$.

The Seebeck coefficient *S*, shown in Fig. 12b, is positive for the samples with 0.0 < x < 0.51 in the whole temperature range indicating the dominant role of holes in the electronic conduction mechanism. The high temperature Seebeck coefficient decreases from 836 μV K^{-1} for x = 0.0 to 12 μV K^{-1} for x = 0.51 at 300 K. Only the Seebeck coefficient of PrCo$_{0.38}$Ni$_{0.62}$O$_3$ exhibits negative values indicating the dominant role of electrons in the electronic conduction mechanism. The observed Seebeck coefficient S_{300K} = 258 μV K^{-1} for x = 0.07 provides an estimate of n_h = 0.049 / M when the classical Heikes formula for the Seebeck coefficient $S_{h,e} = \pm(k/e)\ln\left[(1-n_{h,e})/n_{h,e}\right]$ is applied for hole *h* and electron *e* charge carriers, respectively. Similarly, the observed Seebeck coefficient S_{300K} = 72 μV K^{-1}, 12 μV K^{-1} and -16 μV K^{-1} provide estimates of n_h = 0.302 / M, 0.465 / M and n_e = 0.546 for x = 0.29, 0.49 and 0.62, respectively.

The total thermal conductivity, κ_{total}, of Ni-doped PrCoO$_3$ increases with increasing temperature. At room temperature, κ_{total} is in the range of 1.12 – 1.71 W m^{-1} K^{-1}. The phonon thermal conductivity κ_{ph} varies between 1.02 and 1.62 W m^{-1} K^{-1} at T = 300 K. The phononic part of the thermal conductivity predominates with κ_{ph} > 92 % of the total thermal conductivity. The unusual behavior of the thermal conductivity of PrCoO$_3$ is characterized by three temperature regions. A sudden decrease of the thermal conductivity from κ_{total} = 6.55 W m^{-1} K^{-1} at T = 23 K to 3.38 W m^{-1} K^{-1} at T = 73 K is attributed to phonon – phonon umklapp scattering becoming dominant in this temperature range. In the intermediate temperature region of 73 K < T < 175 K the thermal conductivity increases from 3.38 W m^{-1} K^{-1} to 3.79 W m^{-1} K^{-1}due to crystal-field splitting between the ground state and the first excited level of the Pr^{3+} *4f* shell. A second decrease of the thermal conductivity between 175 K and 294 K is caused by additional phonon scattering due to the spin state transition [24].

The magnetic susceptibility of Ni-doped PrCoO$_3$, was measured in a zero-field-cooled (ZFC) and a field-cooled (FC) regime applying a magnetic field of 0.1 T. The ZFC and FC curves differed considerably which is typical for spin glass materials. With increasing x the effective magnetic moment, determined in the low temperature range of 100 K < T < 150 K based on the Curie-Weiss law, increases up to μ_{eff} = 0.75 μ_B for x = 0.29 and then decreases to μ_{eff} = 0.65 μ_B for x = 0.62. The Weiss constant increases with increasing Ni concentration from Θ = -50 K for x = 0.0 to Θ = 44 K for x = 0.29 and subsequently decreases to Θ = 22 K for x = 0.62 implying that the ferromagnetic interactions are weaker at higher Ni concentrations. These results are in agreement with the electrical transport behavior as the transition between insulating and semiconducting to metallic behavior was observed at Ni contents between 0.29 and 0.49.

The oxidation state of the Co ions was studied by X-ray absorption near-edge structure (XANES)*. The edge position scarcely changes by Ni substitution and for all the samples the nominal oxidation state remains Co^{3+}. As the Ni content increases the edge position (ΔE = -0.6 eV from x = 0.0 to x = 0.62) subtly shifts to lower energies. Also, a reduction of the white line intensity (very small effect) with increasing Ni substitution is observed. Finally, a reduction of the pre-edge intensity can be noticed as the Co content decreases. The pre-edge feature A comes from a quadrupole *1s→3d* transition, which is dipole forbidden. However, the Co-*3d* band is strongly hybridized with the O-*2p* state, providing a *p*-character to the band. These findings, although they could indicate a slight reduction of the Co oxidation state from Co^{3+} to $Co^{3-\delta+}$ with decreasing Co content, are so small that they can be explained by geometrical effects. On the other hand, the Ni *K*-edge position slightly shifts to higher energies (ΔE = + 0.5 eV from x = 0.07 to x = 0.62) as the Co content decreases (Ni content increases from x = 0.07 to x = 0.62). However, as in case of the Co *K*-edge, the nominal oxidation state of the Ni cations is Ni^{3+} in all the samples. A small increase of the intensity of the Ni pre-edge peak with increasing Ni content is observed, too. As stated above, this is rather due to a geometrical effect than to a change in the Ni oxidation state from $Ni^{3-\delta+}$ to Ni^{3+} (accompanying a supposed change in the Co oxidation state).

However, the important decrease in the intensity of the pre-edge peak cannot be explained by reduction from Co^{3+} to $Co^{3-\delta+}$. Figures 13a and b show the change of the pre-edge peaks of the Co and Ni *K*-edges for different Ni contents. It can be observed that with increasing Ni substitution, the intensity of both the Co and Ni pre-edges diminish and even broaden. Moreover, for $PrCo_{0.9}Ni_{0.1}O_3$, no pre-edge in the Ni *K*-edge spectrum can be distinguished. This might be due to the weakening of the Co *3d* – O *2p* hybridization as a consequence of the substitution of Co by Ni. Due to the different relative energy levels of the *3d* band of Co and Ni with respect to the Fermi level (since Ni has one electron more) the O *2p* orbitals spread to cover both *3d* states to form the antibonding *p-d* hybridization with the M-absorber and the M cations at the 3rd coordination sphere. This spreading of the *p-d* hybridized state around the Fermi level results in a broadening and a pre-edge intensity reduction.

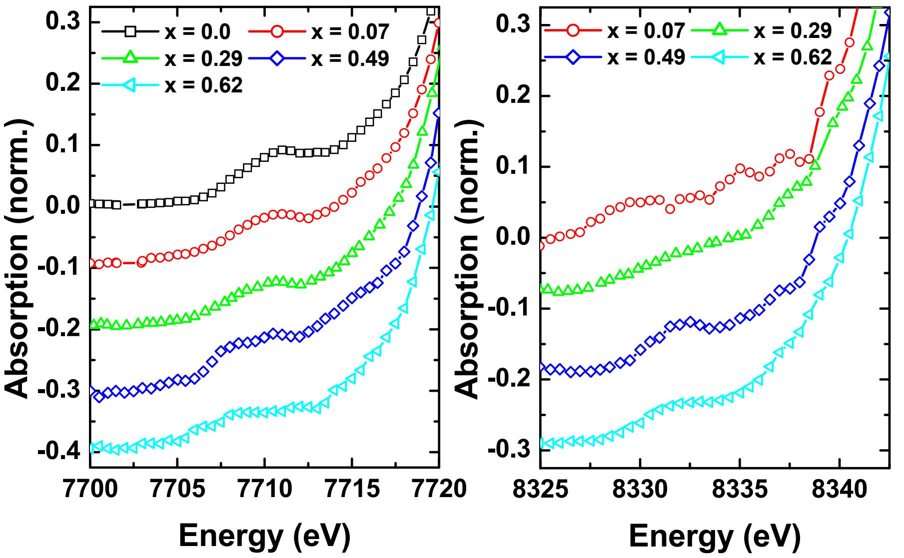

Fig. 13: Pre-edge region of the XANES spectra at the Co *K*-edge and Ni *K*-edge (left and right diagram, respectively) for $PrCo_{1-x}Ni_xO_{3\pm\delta}$ ($0.0 < x < 0.62$).

4.4. $[Ca_2CoO_{3-\delta}]_{0.62}CoO_2$

Magnetotransport measurements were done on a powdered $[Ca_2CoO_{3-\delta}]_{0.62}CoO_2$ single crystal with $T_C \sim 12$ K determined from electrical transport and magnetic data (Fig. 14).The strong negative magnetoresistance (Fig. 14d) and magnetoseebeck effect (Fig. 14b-c) was discovered and evaluated by modified fitting based on the molecular field model [56]. The Seebeck coefficient as the entropy per charge carrier was quenched by a magnetic field. A spin contribution S_{mag} to the Seebeck coefficient S is either due to magnetic interactions and coupling between the local moments and spins of itinerant electrons and/or to spin scattering. The latter often appears e.g. near the magnetic ordering temperature [57].

Further studies on $[Ca_2CoO_{3-\delta}]_{0.62}CoO_2$ as well as on other oxides compounds have to be conducted in order to reveal the origin of the magnetic contribution to the Seebeck coefficient.

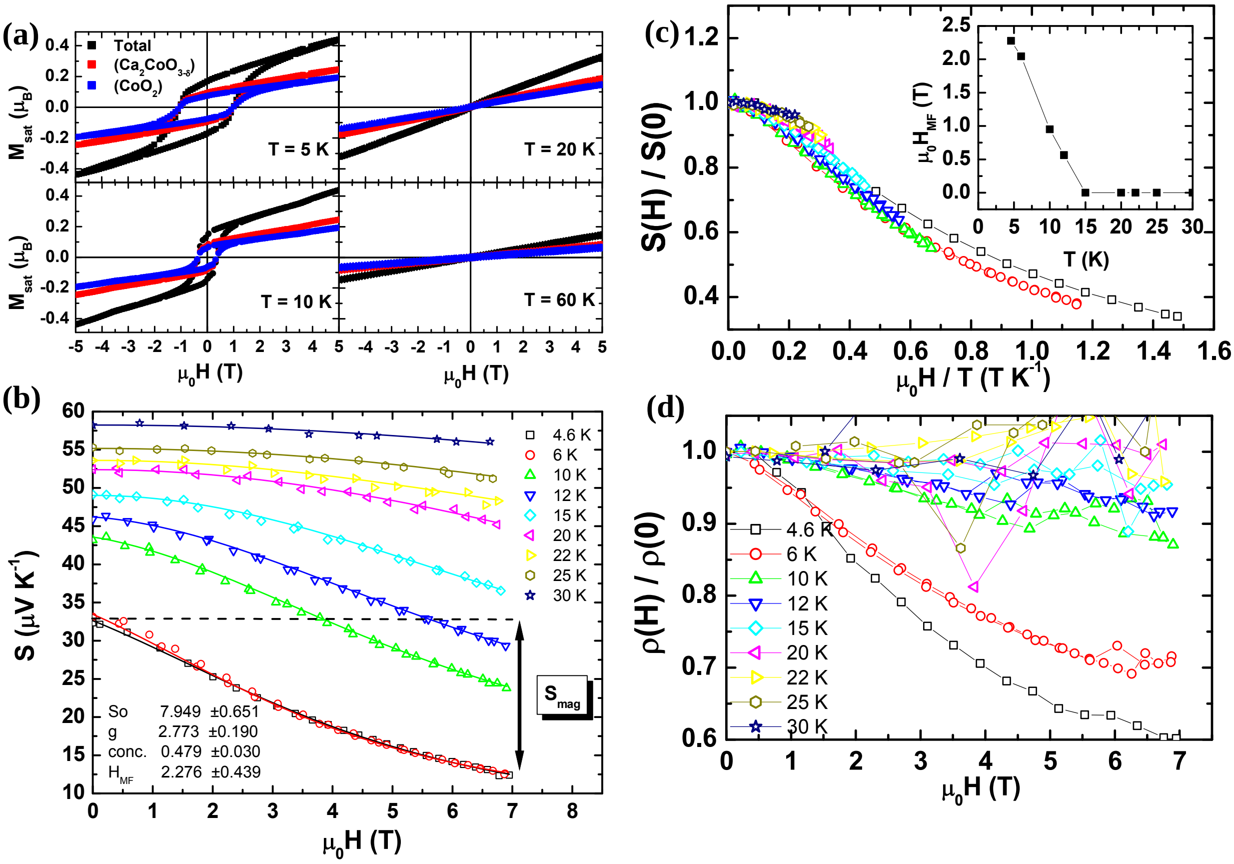

Fig. 14: (a) The magnetohysteresis loops for $[Ca_2CoO_{3-\delta}]_{0.62}CoO_2$, $[Ca_2CoO_{3-\delta}]$ layer, and CoO_2 layer *at* $-5\ T < \mu_0H < 5\ T$ *and T = 5 K, 10 K, 20 K and 60 K. (b) The Seebeck coefficient at* $0\ T < \mu_0H < 7\ T$ *and* $4.6\ K < T < 30\ K$. *(c) The normalized Seebeck coefficient S (H) / S (0) vs.* μ_0H / T. *(d) The normalized electrical resistivity* $\rho (H) / \rho (0)$ *vs.* μ_0H / T.

5. National Collaboration

- A. Bitschi, High Voltage Laboratory, Swiss Federal Institute of Technology, Physikstrasse 3, 8092 Zurich, Switzerland.
- C. Suter, Institute of Energy Technology, ETH Zurich, Sonneggstrasse 3, 8092 Zurich, Switzerland.
- D. Logvinovich, École Polytechnique Fédérale de Lausanne, Laboratoire de Cristallographie, BSP, CH-1015 Lausanne, Switzerland

6. International Collaboration

- J. Hejtmánek, Institute of Physics of ASCR, v.v.i, Laboratory of oxide materials, Na Slovance 2, 182 21 Praha 8, Czech Republic.
- E. Šantavá, Institute of Physics of ASCR, v.v.i, Department of low temperatures, Na Slovance 2, 182 21 Praha 8, Czech Republic.

- F. J. Villacorta, SpLine / Spanish CRG beamline (BM25), European Synchrotron Radiation Facility, F-38043 Grenoble CEDEX, France.
- R. Robert, Grey Solid State Chem. Res. Group, Department of Chemistry SUNY at Stony Brook, USA.

7. References

[1] Alternative energy sources, V.P.M.'s Polytechnic, Thane (2005).

[2] A. Steinfeld, *Sol. Energy* **78**, 603 (2005).

[3] R. A. Meyers, *Encyclopedia of Physical Science & Technology* **15**, 237 (2001).

[4] T. M. Tritt, H. Böttner, and L. Chen, *MRS Bulletin* **33**, (2008).

[5] J. Yang, T. Caillat, *MRS Bulletin* **31**, 224 (2008).

[6] S. S. Kim, F. Yin, Y. Kagawa, *J. Alloys Compd.* **419**, 306 (2006).

[7] O. Yamashita, S. Tomiyoshi, K. Makita, *J. Mater. Sci.* **40**, 6439 (2005).

[8] E. S. Reddy, J.G. Noudem, S. Hebert and C. Goupil, *J. Phys. D: Appl. Phys.* **38**, 3751 (2005).

[9] W. Shin, N. Muruyama, K. Ikeda and S. Sago, *J. Power Sources* **103**, 80 (2001).

[10] R. Funahashi, M. Mikami, T. Mihara, S. Urata and N. Ando, *J. Appl. Phys.* **99**, 066117 (2006).

[11] R. Funahashi, I. Matsubara, H. Ikuta, T. Takeuchi. U. Mizutani and S. Sodeoka, *Japan. J. Appl. Phys.* **39**, L1127 (2000).

[12] R. Funahashi, S. Urata, K. Mizuno, T. Kouuchi and K. Mikami, *Appl. Phys. Lett.* **85**, 1036 (2004).

[13] I. Terasaki, Y. Sasago and K. Uchinokura, Phys. Rev. B 56, R12685 (1997).

[14] M. Ito**,** T. Nagira, D. Furumoto, S. Katsuyama and H. Nagai, *Scr. Mater.* **48**, 403 (2003).

[15] G. Cao, S. McCall, M. Shepard, J. E. Crow, R. P. Guertin, *Phys. Rev. B* **56**, 321 (1997).

[16] M. T. Anderson, K. B. Greenwood, G. A. Taylor, K. R. Poeppelmeier, *Prog. Solid State Chem.* **22**, 197 (1993).

[17] K. Chahara, T. Ohno, M. Kasai, Y. Kozono, *Appl. Phys. Lett.* **63**, 1990 (1993).

[18] Z. Jirák, J. Hejtmánek, K. Knížek, R. Sonntag, *J. Solid State Chem.* **132**, 98 (1997).

[19] P. Tomeš, J. Hejtmánek, K. Knížek, *Solid State Sci.* **10**, 486 (2008).

[20] K. L. Kobayashi, T. Kimura, H. Sawada, K. Terakura, Y. Tokura, *Nature* **395**, 677 (1998).

[21] X. - Y. Zhang, Y. Chen, Z. - Y Li, C. Vittoria, V. G. Harris, *J. Phys.: Condens. Matter* **19**, 266211 (2007).

[22] L. Klein, J. S. Dodge, C. H. Ahn, G. J. Snyder, T. H. Geballe, M. R. Beasley, A. Kapitulnik, *Phys. Rev. Lett.* **77**, 2774 (1996).

[23] S. K. Pandey, A. Kumar, S. Khalid and A. V. Pimpale, *J. Phys.: Condens. Matter* **18**, 7103 (2006).

[24] K. Knížek, Z. Jirák, J. Hejtmánek, P. Novák, *J. Phys.: Condens. Matter* **18**, 3285 (2006).

[25] K. Knížek, Z. Jirák, J. Hejtmánek, M. Veverka, M. Maryško, G. Maris, T. T. M. Palstra, *Eur. Phys. J. B* **47**, 213 (2005).

[26] J.-Q. Yan, J.-S. Zhou, J. B. Goodenough, *Phys. Rev. B* **69**, 144409 (2004).

[27] T. Wu, G. Wu, X. H. Chen, *Solid State Commun.* **145**, 293 (2008).

[28] R. Robert, M. H. Aguirre, L. Bocher, M. Trottmann, S. Heiroth, T. Lippert, M. Döbeli, A. Weidenkaff, *Solid State Sci.* **10**, 502 (2008).

[29] H. Hashimoto, T. Kusunose, T. Sekino, *J. Alloys Compd.* **xxx**, xxx (2009).

[30] K. Sekizawa, M. Kitagawa, Y. Takano, *J. Magn. Magn. Mater.* **177**, 541 (1998).

[31] I. G. Deac, R. Tetean, I. Balasz, E. Burzo, *J. Magn. Magn. Mater.* **xxx**, xxx (2009).

[32] S. K. Pandey, S. Patil, V. R. R. Medicherla, R. S. Singh, K. Maiti, *Phys. Rev. B* **77**, 115137 (2008).

[33] K. Knížek, J. Hejtmánek, Z. Jirák, P. Tomeš, P. Henry, G. André, *Phys. Rev. B* **79**, 134103 (2009).

[34] K. Berggold, M. Kriener, P. Becker, M. Benomar, M. Reuther, C. Zobel, T. Lorenz, *Phys. Rev. B* **78**, 134402 (2008).

[35] G. C. A. M. Janssen, F. D. Tichelaar, C. C. G. Visser, *J. Appl. Phys.* **100**, 093512 (2006).

[36] X. Jin, L. Gao, J. Sun, *Acta Mater.* **54**, 4035 (2006).

[37] C. X. Quintela, F. Rivadulla, J. Rivas, *Appl. Phys. Lett.* **94**, 152103 (2009).

[38] J. D. Browne, P. R. Liddell, R. Street, and T. Mills, *Phys. Status Solidi A* **1**, 715 (1970).

[39] A. Mavromaras, S. Matar, B. Siberchicot, G. Demazeau, *J. Magn. Magn. Mater.* **134**, 34 (1994).

[40] L. M. Corliss, N. Elliott, J. M. Hastings, *Phys. Rev.* **117**, 4 (1960).

[41] D. Hirsch, P. v. Zedtwitz, and T. Osinga, *J. Sol.Energy Eng.* **125**, 117 (2003).

[42] G. J. Snyder, *Appl. Phys. Lett.* **84**, 2436 (2004).

[43] M. A. Bramson, Infrared radiation – A handbook of applications, (1968).

[44] P. Tomeš, R. Robert, M. Trottmann, L. Bocher, M. H. Aguirre, A. Bitschi, J. Hejtmánek and A. Weidenkaff, *J. Electron. Mater.,* **39**, 1696 (2010).

[45] J. Darriet, F. Grasset, P. D. Battle, *Mater. Res. Bull.* **32**, 139 (1997).

[46] B. Dabrowski, O. Chmaissem, P. W. Klamut, S. Kolesnik, M. Maxwell, J. Mais, Y. Ito, *Phys. Rev. B* **70**, 014423 (2005).

[47] Y. Klein, S. Hebert, A. Maignan, S. Kolesnik, T. Maxwell, B. Dabrowski, *Phys. Rev. B* **73**, 052412 (2006).

[48] K. Behnia, D. Jaccard, J. J. Flouquet, *Phys. Condens. Matter* **16**, 5187 (2004).

[49] W.J. Feng, D. Li, W.F. Li, S. Ma, Y.B. Li, D.K. Xiong, W.S. Zhang, Z.D. Zhang, *J. Alloys Compd*. **425**, 4 (2006).

[50] K. Inumaru, K. Koyama, Y. Miyaki, K. Tanaka, and S. Yamanaka, *Appl. Phys. Lett*. **91**, 152501 (2007).

[51] K. Suzuki, T. Kaneko, H. Yoshida, H. Morita, H. Fujimori, *J. Alloys Compd*. **224**, 232 (1995).

[52] M. S. Miao, P. Lukashev, A. Herwadkar, and W. R.L. Lambrecht, *Phys. Status Solidi C* **7**, 2516 (2005).

[53] K. Suzuki, H. Morita, T. Kaneko, H. Yoshida and H. Fujimora, *J. Alloys Compd*. **201**, 11 (1993).

[54] K. Suzukia, T. Kanekob, H. Yoshida, Y. Obi, H. Fujimori, H. Morita, *J. Alloys Compd*. **306**, 66 (2000).

[55] E. Fawcett, *Rev. Mod. Phys*. **60**, (1988).

[56] P. Limette, S. Hébert, V. Hardy, R. Frésard, Ch. Simon, A. Maignan, *Phys. Rev. Lett.* **97**, 046601 (2006).

[57] Y. Wang, N. S. Rogardo, R. J. Cava, N. P. Ong, *Nature* **423**, 425 (2003).

8. Appendix

List of conference contributions and scientific publications in 2009

8.1. Publications

Y. Klein, S. Hébert, A. Maignan, V. Hardy, B. Raveau, B. Dabrowski, P. Tomeš, J. Hejtmánek, Thermoelectric power in ruthenates : Dominant role of the spin degeneracy term, Mater. Res. Soc. Symp. Proc. Vol. 988, 2007.

P. Tomeš, J Hejtmánek, K. Knížek, On the $La_{2-x}Sr_xCoRuO_6$ double perovskites: Crystal structure, magnetic properties and transport, Solid State Sci. 10: 486-490, 2008.

A. Weidenkaff, R. Robert, L. Bocher, P. Tomeš, M. Trottmann, M.H. Aguirre, Perovskite – type thermoelectric oxides and oxynitrides, ECT, Paris, 2008.

P. Tomeš, R. Robert, L. Bocher, M. Trottmann, M. H. Aguirre, A. Weidenkaff, P. Haueter, A. Steinfeld, J. Hejtmánek, Direct conversion of simulated solar radiation into electrical energy by a perovskite thermoelectric oxide module (TOM), Proc. Materials Science and Technology Conference and Exhibition, MS&T08, Pittsburgh, USA, Vol. 1: 429-435, 2008.

D. Logvinovich, J. Hejtmánek, K. Knížek, M. Maryško, N. Homazava, P. Tomeš, R. Aguiar, S. G. Ebbinghaus, A. Reller, A. Weidenkaff, On the magnetism, thermal- and electrical transport of $SrMoO_2N$, J. Appl. Phys: 105, 023522, 2009.

K. Knížek, J. Hejtmánek, Z. Jirák, P. Tomeš, P. Henry, G. André, Neutron diffraction and heat capacity studies of $PrCoO_3$ and $NdCoO_3$, Phys. Rev. B 79, 134103, 2009.

M. Dlouhá, J. Hejtmánek, Z. Jirák, K. Knížek, P. Tomeš, S. Vratislav, Antiferromagnetic ordering in the double perovskites $La_{2-x}Sr_xCoRuO_6$, J. Magn. Magn. Mater. 322, 1189, 2010.

R. Robert, D. Logvinovich, M. H. Aguirre, S. G. Ebbinghaus, L. Bocher, P. Tomeš, A. Weidenkaff, Crystal structure, morphology and physical properties of $LaCo_{1-x}Ti_xO_{3-\delta}$ perovskites prepared by a citric acid assisted soft chemistry synthesis, Acta Mater. 58, 680, 2010.

P. Tomeš, R. Robert, M. Trottmann, L. Bocher, M. H. Aguirre, A. Bitschi, J. Hejtmánek, A. Weidenkaff, Synthesis and Characterisation of New Ceramic Thermoelectrics Implemented in a Thermoelectric Oxide Module, J. Electron. Mater. DOI: 10.1007/s11664-010-1214-4, 2010.

P. Tomeš, K. Knížek, A. Weidenkaff, J. Hejtmánek, On the physical properties of $Sr_{1-x}Na_xRuO_3$ ($x = 0.0 – 0.19$), Solid State Sci. 12, 1112, 2010.

C. Suter, P. Tomeš, M. Trottmann, A. Weidenkaff, and A. Steinfeld, Heat transfer analysis and optimization of thermoelectric converters driven by concentrated solar radiation, Materials 3, 2735, 2010.

D. Logvinovich, A. Arakcheeva, P. Pattison, S. Eliseeva, P. Tomeš, I. Marozau, and G. Chapuis, Crystal structure, optical and magnetic properties of $Pr_2(MoO4)_3$, Inorg. Chem. 49, 1587, 2010.

P. Tomeš, C. Suter. M. Trottmann, M. H. Aguirre, P. Haueter, A. Steinfeld, and A. Weidenkaff, Thermoelectric oxide modules (TOMs) applied in direct conversion of simulated solar radiation into electrical energy, Materials 3, 2801, 2010.

A. Weidenkaff, M. H. Aguirre, L. Bocher, M. Trottmann, P. Tomes, R. Robert, Development of Perovskite-type Cobaltates and Manganates for Thermoelectric Oxide Modules, J. Korean Ceram. Soc. 47, 47, 2010.

S. Ceresara, M. Codecasa, F. Passaretti, P. Tomeš, A. Weidenkaff, C. Fanciulli, Thermoelectric properties of an “in situ” formed $Bi_{0.85}Sb_{0.15}$ / Bi-rich particles composite, J. Electron. Mater, 39, 1696, 2010.

8.2. Conferences

ICT 2010, Thermoelectric oxide modules (TOMs) used in a solar cavity-receiver, Shanghai, 2010 (poster).

Swiss Physical Society, Solar thermoelectric cavity converter, Basel, 2010 (poster).

2010 MRS Spring Meeting, Direct conversion of simulated solar radiation into electrical energy by thermoelectric oxide modules (TOM) with respect to an efficient heat transfer, San Francisco, 2010 (poster).

2009 Swiss Workshop on Materials with Novel Electronic Properties Manep, Thermodynamic, magnetic and transport properties on FM $Sr_{1-x}Na_xRuO_3$ with respect to weak localization effects, Les Diablerets, 2009 (talk).

28th International Conference on Thermoelectrics and 7th European Conference on Thermoelectrics, Thermoelectric and magnetic properties of $PrCo_{1-x}Ni_xO_3$ (x = 0.0 – 0.7), Freiburg 2009 (talk).

2nd Thermopower Symposium CH – 2009: Novel Thermoelectric Materials and Applications, Direct conversion of simulated solar radiation into electrical energy by thermoelectric oxide modules (TOM), Duebendorf 2009 (organisation committee).

33rd International Conference & Exposition on Advanced Ceramics & Composites, Thermoelectric and magnetic properties of $Sr_{1-x}Na_xRuO_3$ (x = 0 – 0.25), Daytona Beach 2009 (talk).

Materials Science & Technology, First full perovskite type oxide thermoelectric module, Pittsburgh 2008 (talk).

The European Materials Research Society, Full perovskite type thermoelectric oxide module, Strasbourg 2008 (talk).

Swiss Physical Society, Evaluation and power generation of p-type $GdCo_{0.95}Ni_{0.05}O_3$ / n-type $CaMn_{0.98}Nb_{0.02}O_3$ thermoelectric oxide modules (TOM), Geneva 2008 (talk).

8.3. Proposals

Valence shift and coordination environment of Co ions in $Pr_{1-x}Sr_xCoO_3$ as function of temperature (ID: CH/2762 BM25A 31-10-2008/04-11-2008, ESRF, Grenoble, Beamline BM25A, 30.10.2008 – 4.11.2008).

Tomography-based determination of the effective transport properties of multiphase materials for solar-driven thermochemical and thermoelectrical processes (ID: 20090143, PSI – SLS, Beamline TOMCAT, 09.10.2009 – 10.10.2009).